

The incommensurately modulated structures of volcanic plagioclase: displacement, ordering and phase transition

Shiyun Jin,^a Huifang Xu,^{a*} Xiaoping Wang,^b Dongzho Zhang,^c Ryan Jacobs^d and Dane Morgan^d

Received 28 December 2018

Accepted 3 May 2019

Edited by M. de Boissieu, SIMaP, France

Keywords: plagioclase; incommensurate structure; displacive; order–disorder; anti-rigid unit mode; *in situ* heating.

CCDC references: 1913810; 1913811; 1913812; 1913813; 1913814; 1913815; 1913816; 1913817; 1913818; 1913819; 1913820; 1913821; 1913822; 1913823; 1913824

B-IncStrDB reference: 14992E63t3B

Supporting information: this article has supporting information at journals.iucr.org/b

^aDepartment of Geoscience, University of Wisconsin-Madison, 1215 W. Dayton Street, Madison, WI 53706, USA,

^bNeutron Scattering Division, Oak Ridge National Laboratory, PO Box 2008 MS-6475, Oak Ridge, TN 37831-6475, USA,

^cGeoSoilEnviroCARS beamline 13-BM-C, Advanced Photon Source, Argonne National Laboratory, 9700 S. Cass Ave, Bldg 434A, Argonne, IL 60439, USA, and ^dDepartment of Materials Science and Engineering, University of Wisconsin-Madison, 1509 University Ave, Madison, WI 53706, USA. *Correspondence e-mail: hfxu@geology.wisc.edu

Four basaltic phenocryst samples of plagioclase, with compositions ranging from An₄₈ (andesine) to An₆₄ (labradorite), have been studied with single-crystal X-ray and neutron diffraction techniques. The samples were also subjected to a heating experiment at 1100°C for two weeks in an effort to minimize the Al–Si ordering in their structures. The average and the modulated structures of the samples (before and after the heating experiment) were compared, in order to understand the mechanism of the phase transition from the disordered C $\bar{1}$ structure to the *e*-plagioclase structure. A comparison between the structures from neutron and X-ray diffraction data shows that the $\langle T-O \rangle$ distance does not solely depend on the Al occupancy as previously thought. A dramatic decrease of the Al–Si ordering is observed after heating at 1100°C for two weeks for all four samples, with an obvious change in the intensities of the satellite reflections (*e*-reflections) in the diffraction pattern. Evident changes in the modulation period were also observed for the more calcic samples. No obvious change in the Ca–Na ordering was observed after the heating experiment. An *in situ* heating X-ray diffraction experiment was carried out on the andesine sample (An₄₈) to study the change in the satellite intensity at high temperature. A dramatic weakening of the satellite peaks was observed between 477°C and 537°C, which strongly supports the displacive nature of the initiation of *e*2 ordering. Rigid-Unit Mode (RUM) analysis of the plagioclase structure suggests the initial position of the *e*-reflections is determined by the anti-RUMs in the framework.

1. Introduction

Plagioclase feldspars, the solid solution series between albite (Ab, NaAlSi₃O₈) and anorthite (An, CaAl₂Si₂O₈), are the most common rock-forming minerals in the Earth's crust. The crystal structure of feldspar consists of a 3D-interconnected Al–Si tetrahedral framework, with larger cations (Ca, Na and K) filling the interstitial spaces. The coupled substitution between Na+Si and Ca+Al in plagioclase solid solution results in a continuous variation of the Al/Si ratio, creating dramatically different ordering patterns in the tetrahedral framework as a function of the composition. The low-temperature plagioclase of intermediate composition (An₂₅ to An₇₅) has an incommensurately modulated structure that displays satellite diffractions (*e*-reflections) surrounding the absent *b*-positions ($h+k = \text{odd}, l = \text{odd}$) and are, therefore, called *e*-plagioclases. The *e*-plagioclase structures are categorized into two groups, *e*1 and *e*2, based on the existence of *f*-reflections, which indi-

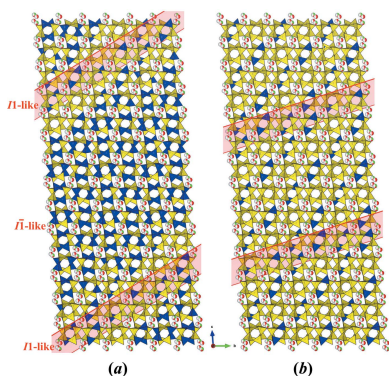


Table 1

Composition, provenance and brief description of the samples used in this study.

Sample	Composition†	Locality	Description	Structure	References
Hogarth Range	An ₄₈ Ab ₄₉ Or ₃	Hogarth Range, Australia	1–2 cm-sized phenocrysts in basalt, yellow, transparent and clear, most crystals are crack free	Very diffuse peak at <i>e</i> -position Weak and diffuse <i>e</i>	Fitz Gerald <i>et al.</i> (1986)
MXCG	An ₅₈ Ab _{40.5} Or _{1.5}	Casas Grandes, Mexico		Weak and diffuse <i>e</i>	Jin, Wang & Xu (2018)
96GM1	An _{60.5} Ab _{37.5} Or ₂	Steens Mtn, Oregon, USA		Weak and diffuse <i>e</i>	Langer (1991)
Lake County sunstone	An ₆₄ Ab ₃₅ Or ₁	Lake County Oregon, USA		Weak, slightly diffuse <i>e</i> , very close together	Stewart <i>et al.</i> (1966), Wenk <i>et al.</i> (1980), Jin, Wang & Xu (2018)

† Or (orthoclase) indicates the K percentage in the composition.

cate density modulation in the structure (Smith, 1984; Carpenter, 1994; McConnell, 2008; Jin & Xu, 2017b).

Recent studies have greatly improved our understanding of this complicated binary system. Xu *et al.* solved and refined the *e*1 structure (Xu *et al.*, 2016; Jin & Xu, 2017b), and provided an accurate and detailed description of the incommensurate structure, which matches the direct STEM observation by Xu (2015). Jin & Xu (2017c) confirmed the differences between the *e*1 and *e*2 structures, based on the complete extinction of *f*-reflections and different *q*-vectors in the *e*2 structure with the same composition. They also discovered how different cooling rates of the host rock affect the final modulated structure of *e*-plagioclase with the same composition, where the *e*2 structure may appear as a metastable phase with a Ca-rich composition. Jin & Xu (2017a) made a comprehensive study of the modulated structures of a Na-rich plagioclase over 11 samples, and accurately defined the phase boundary between the *e*1 and *e*2 phases.

This progress on the study of *e*-plagioclase improved our knowledge of the equilibrium subsolidus phase relations. However, the ordering process from the disordered $C\bar{1}$ structure to *e*-plagioclase is still unclear. Many different mechanisms have been proposed over the years to explain the formation of the aperiodic but ordered structure in plagioclase feldspars (Smith & Ribbe, 1969; Grove, 1977; Kitamura & Morimoto, 1977; Nakajima *et al.*, 1977; Wenk & Nakajima, 1980; Horst *et al.*, 1981; Grove *et al.*, 1983; Horst, 1984; Kumao *et al.*, 1987). However, almost all of them are based on unsubstantiated assumptions, such as the instability of *e*-plagioclase or inaccurate structural models. As the accurate structural model of *e*-plagioclase has been solved, and its stable area in the phase diagram has been revealed, most previously proposed mechanisms of the formation of incommensurate plagioclase feldspars have been rendered invalid.

To understand the detailed process of the structural transition from the disordered $C\bar{1}$ structure to *e*-plagioclase, it is informative to examine structures that represent an intermediate stage between $C\bar{1}$ structure and *e*2 structure. The closest samples representing this intermediate stage found in nature are the plagioclase phenocrysts in volcanic rocks. These plagioclase samples are crystallized near their melting temperature, and float in the magma at high temperature until volcanic eruption. These phenocrysts then cool down rapidly under ambient temperature (exact rate depends on the thickness of the lava flow), therefore, mostly preserving the disordered structure at high temperature. Minor ordering may

happen during the cooling period that may last days or even weeks. Plagioclase phenocrysts in volcanic rocks have actually been a popular subject in the research of the solid solution series, mainly due to their sample size and purity (Stewart *et al.*, 1966; Rainey & Wenk, 1978; Wenk, 1978; Wenk *et al.*, 1980; Fitz Gerald *et al.*, 1986; Tagai & Korekawa, 1981; Tagai *et al.*, 1978). Meanwhile, most studies on volcanic plagioclase samples are qualitative due to the weak intensities of the satellite peaks in the diffraction pattern. In this work, we collected several plagioclase phenocryst samples with different compositions from different locations. Our combined use of single-crystal X-ray and neutron diffraction techniques, heating experiments (both for long time periods and *in situ* with the diffraction experiments) and Rigid-Unit-Mode (RUM) analysis provides a deeper understanding of the mechanism behind the complicated phase transition of the disordered $C\bar{1}$ and the incommensurately ordered *e*2-plagioclase structures.

2. Sample and experiment

Four volcanic plagioclase phenocryst samples from Australia, Mexico and Oregon (USA) were studied in this work. The compositions, localities, brief descriptions and of these samples are given in Table 1. All the samples studied are transparent and clear with no oxide inclusions. They have almost the same appearance and it is difficult to discern one from another without chemical analysis. Twinning is rarely found in these volcanic phenocrysts, which makes sample preparation straightforward. The single crystals for X-ray diffraction were picked from crushed pieces of the samples. The Mexican sample was also cut along the (010), (001) and (40 $\bar{3}$) (approximately perpendicular to the *a*-axis) planes into a 2 mm × 2 mm × 2 mm cube, for use in neutron diffraction. The chemical composition of the samples was analysed using a CAMECA SXFive field emission electron microprobe at 15 kV and 10 nA beam current with a 20 μm beam size. Plagioclase and iron oxide standards were used in the microprobe analysis and the results are listed in Table S1.

Crystal fragments (0.1–2 mm) of the samples studied were dry-heated at 1100°C in air in a standard muffle furnace for two weeks. The heated crystals were then quenched to room temperature in air after the heating experiment. Complete data sets from single-crystal X-ray diffraction were collected for before and after the annealing experiment, though not on exactly the same crystals.

Table 2

Experimental and refinement details of the average structures from X-ray and neutron diffraction.

	Hogarth Range		MXCG		96GM1		Lake County		
	Untreated	Annealed	Untreated	Annealed	Untreated	Annealed	Untreated	Annealed	
Crystal data									
Chemical formula	Ca _{0.48} Na _{0.52} Al _{1.48} Si _{2.52} O ₈		Ca _{0.58} Na _{0.42} Al _{1.58} Si _{2.42} O ₈		Ca _{0.61} Na _{0.39} Al _{1.61} Si _{2.39} O ₈		Ca _{0.64} Na _{0.36} Al _{1.64} Si _{2.36} O ₈		
<i>a</i> , <i>b</i> , <i>c</i> (Å)	8.1594 (1), 12.8639 (1), 7.1038 (1)	8.1627 (3), 12.8630 (2), 7.1003 (2)	8.1603 (1), 12.8614 (1), 7.0987 (1)		8.1615 (1), 12.8617 (1), 7.0987 (1)	8.1625 (1), 12.8629 (1), 7.0998 (1)	8.1651 (2), 12.8649 (1), 7.0978 (1)	8.1612 (1), 12.8651 (1), 7.0971 (1)	8.1628 (6), 12.8610 (4), 7.0992 (4)
α , β , γ (°)	93.5384 (6), 116.2056 (9), 90.2802 (13)	93.539 (1), 116.150 (2), 90.385 (3)	93.5343 (7), 116.1173 (10), 90.4341 (13)		93.5469 (7), 116.102 (1), 90.4797 (13)	93.5170 (6), 116.1301 (9), 90.4248 (13)	93.5430 (7), 116.084 (1), 90.4555 (14)	93.5263 (5), 116.1069 (5), 90.5072 (13)	93.570 (2), 116.073 (3), 90.534 (5)
<i>V</i> (Å ³)	667.28 (1)	667.45 (3)	667.35 (2)		667.49 (1)	667.85 (2)	667.33 (1)	667.58 (7)	667.28 (1)
Crystal size (mm)	0.09 × 0.12 × 0.15	0.09 × 0.18 × 0.19	0.05 × 0.07 × 0.14 (X-ray)	2 × 2 × 2 (neutron)	0.11 × 0.15 × 0.16	0.14 × 0.15 × 0.24	0.10 × 0.17 × 0.22	0.07 × 0.15 × 0.21	0.10 × 0.10 × 0.15
Data collection									
Exposure (s)	60	35	75	7 (C per scan)	35	105	35	30	80
Scanning width (°)	0.5	0.5	0.5	N/A	0.5	0.5	0.5	0.5	0.5
Runs	4 ω +1 φ	3 ω +1 φ	3 ω +1 φ	25	3 ω +1 φ	3 ω +1 φ	3 ω +1 φ	11 ω	3 ω +1 φ
No. of total reflections	7754	6308	6363	16 363	6347	6005	6293	14 567	6451
No. of independent reflections	2033	2020	2029	16 363†	2025	1988	2026	2038	2036
No. of observed [<i>I</i> > 3 σ (<i>I</i>)]	1922	1960	1864	15 814	1915	1943	1931	1948	1947
<i>R</i> _{int}	0.084	0.016‡	0.061	0.046	0.048	0.076	0.054	0.067	0.022‡
θ_{\max} , θ_{\min} (°)	30.5, 3.2	30.5, 3.2	30.5, 3.2	78.4, 7.5	30.5, 3.2	30.5, 3.2	30.5, 3.2	30.5, 3.2	30.7, 3.2
($\sin \theta/\lambda$) _{max} (Å ⁻¹)	0.715	0.715	0.715	1	0.714	0.714	0.715	0.714	0.717
<i>h</i>	−11→11	−11→11	−11→11	−16→14	−10→11	−11→11	−11→11	−11→11	−10→11
<i>k</i>	−18→18	−18→18	−18→17	−25→25	−18→18	−18→18	−18→18	−18→18	−18→18
<i>l</i>	−10→10	−9→10	−10→10	−14→14	−10→8	−10→10	−10→10	−10→10	−10→9
Refinement									
<i>R</i> (obs)	0.028	0.024	0.025	0.058	0.023	0.028	0.024	0.026	0.022
<i>R</i> (all)	0.106	0.108	0.089	0.168	0.092	0.117	0.094	0.111	0.095
GOF(all)	2.31	2.36	1.79	1.38	2	2.76	2.06	2.5	2.03
GOF(obs)	2.35	2.37	1.86	1.38	2.03	2.78	2.1	2.55	2.07
No. of parameters	127	127	127	158	127	127	127	127	130
No. of constraints	59	59	59	0	59	59	58	59	59
$\Delta\rho_{\max}$, $\Delta\rho_{\min}$ (e Å ⁻³)	0.59, −0.71	0.55, −0.60	0.53, −0.33	1.61, −2.43	0.54, −0.36	0.44, −0.41	0.49, −0.34	0.59, −0.64	0.51, −0.33

† Each reflection is treated as an independent reflection from time-of-flight Laue neutron diffraction because the reflections that have the same or equivalent *hkl* are almost certainly from different wavelengths, which is a factor in the absorption correction. ‡ The significantly lower *R*_{int} value results from performing absorption correction with the *APEX3* program, instead of using the .raw file. The samples are all weak absorbers, so this does not affect the refinement much. It was done to avoid some negative occupancies in the *M* site.

X-ray diffraction data were collected on a Bruker Quazar APEXII single-crystal diffractometer with an Mo *K* α I μ S source and a APEXII detector. For each sample, 3–4 ω runs and 1–2 φ runs with a scan width of 0.5° were programmed in order to obtain a full coverage of data up to 0.7 Å. The instrument ran at a voltage of 50 kV and current of 0.6 mA. The detector was at a distance of 5 cm from the crystal. Unit-cell parameters were calculated and refined using Bruker *APEX3* software. The single-crystal neutron diffraction data were collected at BL-12 (TOPAZ) of Spallation Neutron Source (SNS) in Oak Ridge National Laboratory. The data collection strategy was calculated and optimized with the *CrystalPlan* software (Zikovskiy *et al.*, 2011) using the orientation matrix obtained from the initial sample orientation. Twenty five scans were planned to acquire data sets with more than 95% completeness with a resolution of 0.5 Å. Detected neutrons were stored as events with associated time of

detection, detector and pixel information. The data were collected with a proton charge of 7 Coulombs for each scan. Data were displayed, auto-indexed and integrated using the suite of algorithms in *Mantid* (Arnold *et al.*, 2014). These events were transformed into *Q*-space and integrated using a 3D ellipsoid fitted to each reflection in accordance with previously reported methods (Schultz *et al.*, 2014). The integrated intensities were then scaled and corrected for detector efficiency, the spectrum of the incident beam and Lorentz factors with the *ANVRED3* program (Schultz *et al.*, 1984). Absorption corrections, assuming spherical samples, were also applied in *ANVRED3*. The X-ray and neutron diffraction data were both collected at 100 K.

Single-crystal X-ray diffraction at various temperatures was carried out at the experimental station 13-BM-C of the Advanced Photon Source, Argonne National Laboratory (Zhang *et al.*, 2017). The X-ray beam was monochromated to

Table 3
Experimental and refinement details of the modulated structures from X-ray diffraction.

	MXCG	MXCG annealed	96GM1	96GM1 annealed	Lake County	Lake County annealed
Crystal data						
<i>a</i> , <i>b</i> , <i>c</i> (Å)	8.1603 (1), 12.8612 (1), 14.1976 (2)	8.1615 (1), 12.8620 (1), 14.1974 (2)	8.1626 (3), 12.8622 (2), 14.1986 (4)	8.1652 (2), 12.8647 (1), 14.1954 (2)	8.1617 (1), 12.8657 (1), 14.1946 (2)	8.1628 (6), 12.8607 (4), 14.1988 (8)
α , β , γ (°)	93.5340 (7), 116.1177 (10), 90.4332 (13)	90.4806 (13), 116.1018 (9), 90.4806 (13)	93.5118 (10), 116.1302 (12), 90.421 (3)	93.5426 (7), 116.0848 (11), 90.4563 (14)	93.5226 (5), 116.1052 (5), 90.5088 (13)	93.569 (2), 116.075 (3), 90.534 (5)
<i>V</i> (Å ³)	1334.36 (3)	1334.73 (3)	1334.85 (7)	1335.66 (4)	1334.86 (3)	1335.15 (13)
Wavevectors	0.0416 (12) 0.0691 (12) −0.1582 (7)	0.0416 (12)† 0.0691 (12) −0.1582 (7)	0.06566 (15) 0.06422 (15) −0.20738 (7)	0.0478 (15) 0.0560 (15) −0.2532 (9)	0.02390 (18) 0.05652 (18) −0.09524 (7)	0.0402 (18) 0.0559 (18) −0.1768 (8)
Modulation period (Å)	41.3	~30	32.7	27.4	64.1	38.6
Data collection						
No. of total reflections	19 266	19 368	18 782	19 305	12 250	10 395
No. of independent reflections‡	6101 (2031+4070)	6093 (2028+4065)	6063 (1994+4069)	6098 (2029+4069)	6134 (2038+4096)	6115 (2036+4079)
No. of observed [<i>I</i> > 3 σ (<i>I</i>)]‡	2362 (1864+498)	2169 (1918+251)	3938 (1951+1987)	2318 (1930+388)	4427 (1960+2467)	2722 (1924+798)
<i>R</i> _{int} ‡	0.064 (0.061, 0.214)	0.048 (0.048, 0.236)	0.077 (0.076, 0.144)	0.055 (0.055, 0.172)	0.009 (0.008, 0.057)	0.013 (0.012, 0.151)
θ_{\max} , θ_{\min} (°)	30.6, 2.0	30.5, 2.0	30.5, 1.9	30.5, 1.9	30.6, 2.0	30.7, 2.0
(<i>sin</i> θ / λ) _{max} (Å ^{−1})	0.715	0.715	0.715	0.715	0.715	0.719
<i>h</i>	−11→11	−10→11	−11→11	−11→11	−11→11	−10→11
<i>k</i>	−18→17	−18→18	−18→18	−18→18	−18→18	−18→18
<i>l</i>	−20→20	−20→17	−20→20	−20→20	−20→20	−20→19
Refinement						
<i>R</i> (obs)‡	0.030 (0.026, 0.133)	0.025 (0.024, 0.147)	0.046 (0.034, 0.151)	0.028 (0.025, 0.145)	0.040 (0.026, 0.109)	0.031 (0.024, 0.191)
<i>R</i> (all)‡	0.105 (0.091, 0.334)	0.103 (0.094, 0.435)	0.175 (0.126, 0.315)	0.109 (0.098, 0.376)	0.146 (0.101, 0.234)	0.125 (0.098, 0.395)
GOF(all)	1.24	1.3	2.61	1.39	2.21	1.54
GOF(obs)	1.92	2.13	3.16	2.23	2.56	2.18
No. of parameters	384	384	384	384	384	384
No. of constraints	151	151	151	151	151	151
$\Delta\rho_{\max}$, $\Delta\rho_{\min}$ (e Å ^{−3} or f Å ^{−3})	0.87, −0.69	0.61, −0.57	0.86, −0.87	0.58, −0.54	0.94, −0.66	0.88, −0.72

† The *q*-vector of the annealed MXCG sample used in the refinement is the same as the untreated sample. Because relaxing the *q*-vector in the data integration does not produce reasonable value, due to the weaker and diffuser *e*-reflections in the annealed sample. The satellite intensity should be reliable, because even though the fixed *q*-vector does not match the satellite peak position exactly, the box size for integration should be large enough to cover the satellite peak. ‡ The numbers in the parenthesis are those for the main *a*-reflections and satellite *e*-reflections, respectively; also the same for the *R*_{int} and *R* value in the refinement result.

28.6 keV (0.434 Å), with a 1 eV bandwidth. A Kirkpatrick–Baez mirror system focused the X-ray to a spot size of 12 (H) μm × 18 (V) μm, measured at the full width at half-maximum. The MAR165 CCD detector (Rayonix) was placed ~170 mm away from the sample and the calibrated LaB₆ powder (NIST) was used to calibrate the distance and tilting of the detector. The sample was placed on the rotation centre of the diffractometer and aligned using an optical microscope. A miniature resistive heater was used to heat the sample (Chupas *et al.*, 2008) and a K-type thermocouple was placed close to the sample to read the temperature. The plagioclase crystal was mounted in a fused silica glass capillary, by pushing the crystal from the thicker end, until it could not move further.

Refinement of the structures was carried out with *JANA2006* (Petříček *et al.*, 2014) on *F*², with a weighting scheme based on measured standard uncertainties, $w = 1/[\sigma^2(I) + 0.0016I^2]$. Structure refinements with neutron data were also made with the cell parameters from the X-ray diffraction for comparison, because the results of the cell parameters from X-ray diffraction are much more accurate with a smaller crystal and beam size than for those from neutron diffraction.

The 3D crystal structure was visualized by *VESTA* (Momma & Izumi, 2011). The lattice parameters of the samples and some details of data and structure refinements are listed in Tables 2 and 3.

3. Diffraction data

Previous studies have shown us the importance of examining the raw data before trying to solve and refine the structure (Jin, Wang & Xu, 2018; Jin, Xu *et al.*, 2018). Without this first step, the data may be reduced in a completely wrong space group which would inevitably lead to an incorrect structure. Sections of the unwrapped precession images of the *0kl* plane from the X-ray diffraction data are shown in Fig. 1. A slice of the same orientation through the *hkl* (reciprocal) space from the neutron diffraction data of sample MXCG is also provided in Fig. S1.

The diffraction pattern of each of the samples studied in this work clearly shows *e*-reflections, indicating an incommensurately modulated structure. The intensities of the satellite reflections increase with mol% An in the composition. The *e*-reflections of the Hogarth Range sample are the most

separated, indicating the shortest modulation period, and those of the Lake County sunstone sample are closest together, indicating the longest modulation period. Sample 96GM1 shows a shorter modulation period compared to sample MXCG even though the mol% An number is higher. As suggested by Jin & Xu (2017*a,c*), composition is not the only factor that affects the modulation direction and period of the *e*-plagioclase structures. After annealing at 1100°C, all the *e*-reflections become noticeably weaker and more diffuse. More interestingly, the positions of the *e*-reflections noticeably move further away from one another. The modulation period of the Lake County sunstone sample dropped from ~64 Å to ~39 Å after heating.

Rainey & Wenk (1978) suggested that the relative intensities of certain subsidiary reflections can be helpful for categorizing the plagioclase structures. Intensity ratios of (071)/(073) versus (093)/(095) are plotted in Fig. 2, following Rainey & Wenk (1978). The intensity ratios of the four $\bar{1}\bar{1}$ structures from Jin, Wang & Xu (2018) are also included for comparison. It is clear that the ratios of the Hogarth Range, MXCG and 96GM1 samples lie within the *e*-plagioclase region defined by Rainey & Wenk (1978). The intensity ratio of the Lake County sample used in this work lies much closer to the *e*-plagioclase area compare to the one used by Rainey & Wenk (1978). Since almost pure $\bar{1}\bar{1}$ structures are also found in other phenocryst samples from the Lake County of Oregon State (Jin, Wang & Xu, 2018) (yellow square in Fig. 2), it should not be surprising if the whole spectrum between the $\bar{1}\bar{1}$ structure and *e*-plagioclase can be found in crystals from Lake County. As for the sample used in this work, we will treat it as a pure *e*-plagioclase structure, since the satellite reflections are quite sharp and obviously separated [Fig. 1(*d*)]. No second or higher order satellite reflections were observed in the X-ray diffraction pattern for any of the crystals studied in this work; therefore

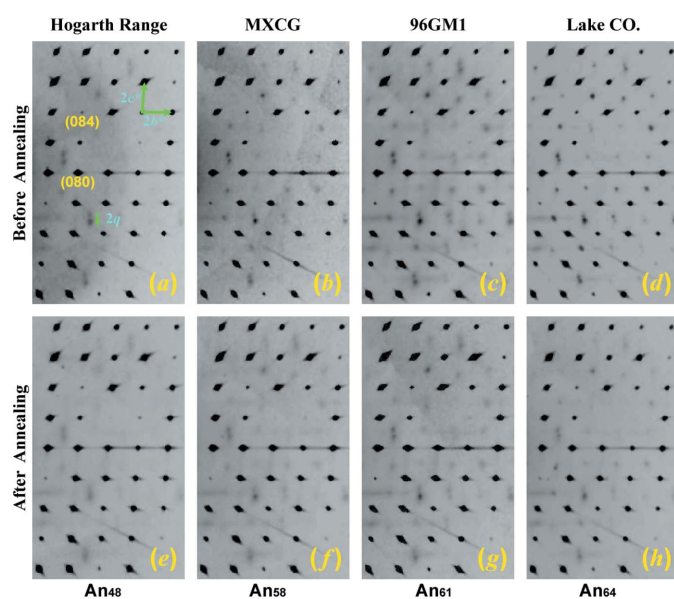


Figure 1
Fractions of the $0kl$ precession images from X-ray diffraction data. The sample name and compositions are labelled above and below the figure, respectively.

they should all be characterized as the *e*2 structure even with Ca-rich compositions (Jin & Xu, 2017*c*).

4. Structure refinement

4.1. Average structure

The average structures of all the samples were refined with only the *a*-reflections. This was done to maintain consistency in the comparisons between the structures, because the satellite reflections of the Hogarth Range sample, both before and after heating, are too weak to refine the modulation in the structure. Only Ca and Na atoms were used in the refinement, and the chemical formula of the structure was constrained based on the chemical analysis result (K component from microprobe analysis is attributed to Na in the refinement to keep the charge balanced). The same structure model reported by Fitz Gerald *et al.* (1986) was used, with two partially occupied *M* sites. The Ca and Na occupancies of each *M* site in the Hogarth Range sample were constrained with the result from Fitz Gerald *et al.* (1986). With both single-crystal X-ray and neutron diffraction data for sample MXCG, the Ca and Na occupancy of each *M* site was calculated in the same way as reported by Fitz Gerald *et al.* (1986) and Jin, Wang & Xu (2018). However, in contrast to the conclusions given by Fitz Gerald *et al.* (1986), the Ca/Na ratio of each *M* site is basically the same as the bulk composition of the crystal, with no obvious preference of Na atoms towards the *M*1 site observed. The Al occupancies of the *T* sites were estimated from the $\langle T-O \rangle$ bond distances, except for sample MXCG in which the Al occupancies were directly refined from the neutron diffraction data. We found the surprising result that

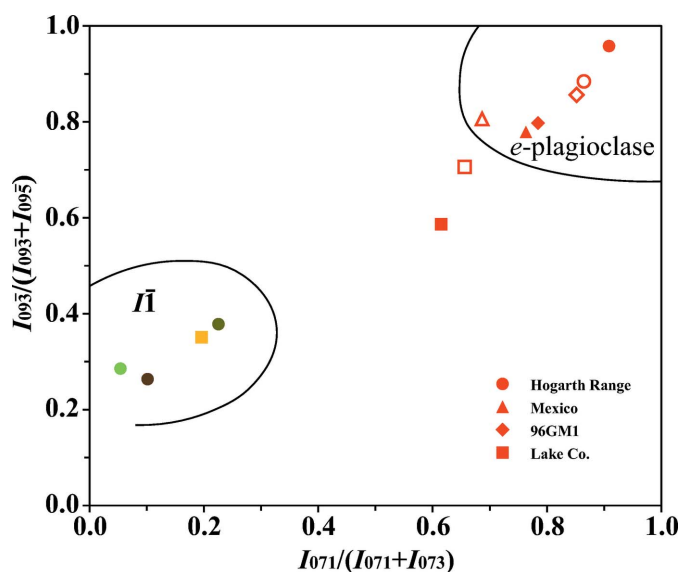


Figure 2
A plot of intensity ratios (093)/(095) versus (071)/(073) for the samples studied in this work. Data points from the $\bar{1}\bar{1}$ structures given by Jin, Wang & Xu (2018) are also plotted for comparison. The samples in this work are coded in red and the $\bar{1}\bar{1}$ structures are kept the same as in the original paper. The filled and empty points indicate the structure before and after the heating experiment, respectively.

even though the $\langle T_{1o}-O \rangle$ distance is obviously longer than $\langle T_{1m}-O \rangle$ distance, the Al occupancy is lower in T_{1o} site from neutron diffraction data. Although it seems the exact outcome of the Al occupancies depends on the weighting scheme used in the refinement, the neutron data strongly suggest the Al–Si ordering in the volcanic plagioclase does not linearly correlate with the $\langle T-O \rangle$ distance as commonly believed. The larger T_{1o} site is not a result of higher Al occupancy, but more likely the reverse. The T_{1o} tetrahedron is probably forced to be larger by the geometry from the transition from a monoclinic ideal structure and Al–Si ordering is simply a consequence of this geometric feature, as Al energetically prefers a larger tetrahedral site. This could also potentially explain the absence of albite twins in these basaltic phenocrysts, which is almost ubiquitous in plutonic and metamorphic plagioclase crystals. The plagioclase phenocrysts grow in basaltic magma, which is a strain-free liquid environment. The disordered T_{1o}/T_{1m} sites make the framework topologically monoclinic, as there is no chemical difference between all the T_1 sites. These conditions would practically make a twin boundary unsustainable. The few albite twins observed in the phenocryst samples are most likely induced by the strain during the solidification of the basaltic lava.

Another detail of interest from the average structure is that regarding the M site of sample MXCG refined from neutron diffraction data. The electron density map (from X-ray diffraction) and the nuclear density map (from neutron diffraction) are shown in Fig. 3 from two different projections (a -axis and c^* -axis). The $M1$ site in the nuclear density map is particularly elongated, even though the electron density map shows a normal near-spherical shape. This is hardly surprising considering that the position of the $M1$ site is modulated in the real structure, and neutron diffraction is more sensitive (than

X-ray diffraction) to the position of atoms. However, the nuclear density map of the $M1$ site seems to fit better to two atoms (resulting in three split M sites in total), which cannot be explained by the positional modulation of the atoms. The satellite reflections in the neutron diffraction data from sample MXCG (Fig. S1) are too weak for us to say anything conclusive about the modulated structure; therefore, they were not used in the refinement. Nonetheless, this detail raises the question about the exact configuration of the M site in e -plagioclase structures and whether neutron diffraction can provide information that cannot be obtained from X-ray diffraction. To answer this question, a sample with much stronger modulation and perhaps a longer exposure time under the neutron beam would be needed.

4.2. Modulated structures

As mentioned above, the samples studied in this work are all considered to be $e2$ structures with no density modulation. The modulated structure model used in the refinement is the same as Dul-15-8B (Jin & Xu, 2017c), as well as 89GM69 and T-12-22a (Jin & Xu, 2017a). As discussed by Jin & Xu (2017c), the main difference between the structures of $e1$ and $e2$ is that only simple harmonic functions are present in $e2$ structures, whereas higher order harmonic functions are used in $e1$ structures. The M site is refined as two split sites, $M1$ and $M2$, with $M2$ only occupied by Ca and $M1$ containing both Ca and Na. The total occupancy of the atoms in $M1$ and $M2$ sites is constrained to 1, and the average Na occupancy is fixed according to the chemical analysis of the sample. All atoms were refined with first-order harmonic positional modulation. The modulation of atomic displacement parameters is also allowed for all atoms in the refinement. The occupancies of tetrahedral sites were calculated based on the modulation of $\langle T-O \rangle$ bond distances, the same as previously published

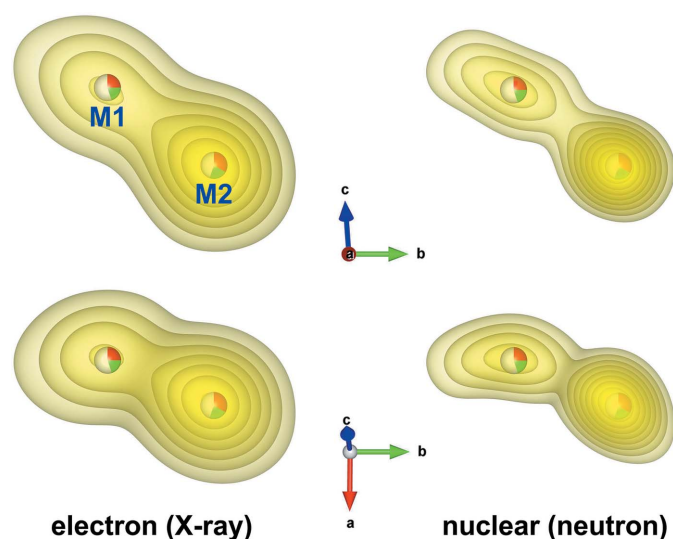


Figure 3 3D contoured density maps around the M site in sample MXCG, viewed along the a -axis (top figures) and the c^* -axis (bottom figures). The nuclear density map from neutron diffraction data provides more detailed information regarding the atom positions in the structure, compared to the electron density map from X-ray diffraction data.

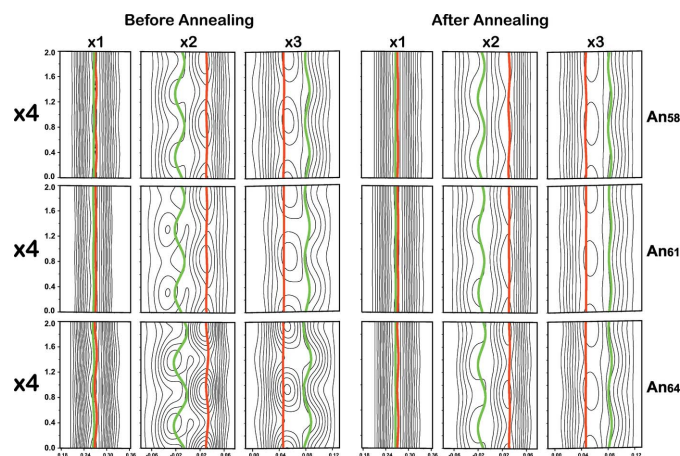


Figure 4 The displacement modulation of M site along three axes of the three samples (MXCG-An₅₈, 96GM1-An₆₁ and Lake County-An₆₄) studied in this work. The modulation before and after the two-week heating are compared side-by-side with the original structure on the left and the post-heating structures on the right.

refinements of *e*-plagioclase structures. The equation by Kroll & Ribbe (1983) is used:

$$\text{Occ}(\text{Al})_i = 0.25(1 + n_{\text{An}}) + ((T_i - O) - \langle T - O \rangle)/k,$$

where the value of *k* is estimated to be 0.135 (Angel *et al.*, 1990; Jin & Xu, 2017*a,b,c*).

The positional modulation of the *M* site along with contoured electron density change are plotted in Fig. 4. Similar to the previously published modulated structures (Jin & Xu, 2017*a,b,c*), the *M*2 site (Ca) is nearly stationary, with the *M*1 site (Na+Ca) displaced further and closer relative to the *M*2 site over the modulation period. The amplitude of the modulation increases with the composition from sample MXCG to the Lake County sunstone sample. The modulation after heating is observably weakened for each sample.

The *M*-site occupancy modulations of the structures are plotted in Fig. 5. All the samples show minor amplitude in the occupational modulations. The Na occupancy, which is a function of the total scattering power of *M*1 and *M*2, is essentially constant in the modulated structure. This means there is basically no Ca–Na ordering in the *M* sites of the structure. The Ca occupancy shows slightly higher amplitude,

indicating some change in the distribution between *M*1 and *M*2 site. However, it is still hard to say if this modulation is real or just from the imperfections of the crystal and the errors from data collection. If the occupancy modulation is disabled in the refinement, the resulting structure barely changes with very similar *R*-factor. What is more certain, however, is that heating the sample did not considerably change the *M*-site occupancy. The Ca occupancy modulation in the Lake County sunstone sample, which is the most ordered among the samples studied in this paper, shows some phase shift compared to the other samples. This phase shift most likely results from the minor $\bar{1}\bar{1}$ component in the sample, as indicated by the intensity ratio plot (Fig. 2) and previously published results. The structure after heating is the same as the other samples, suggesting the $\bar{1}\bar{1}$ -ordered component is eliminated (or at least reduced) during the annealing experiment.

The $\langle T-O \rangle$ bond distance modulation, illustrated in Fig. 6, reveals something more interesting. Confirming the observation by Jin & Xu (2017*a,c*), the wavefunctions of different samples have the same structure, despite the differences in compositions and *q*-vectors, and the only thing that varies is the amplitude. Sample 96GM1 and sample MXCG show

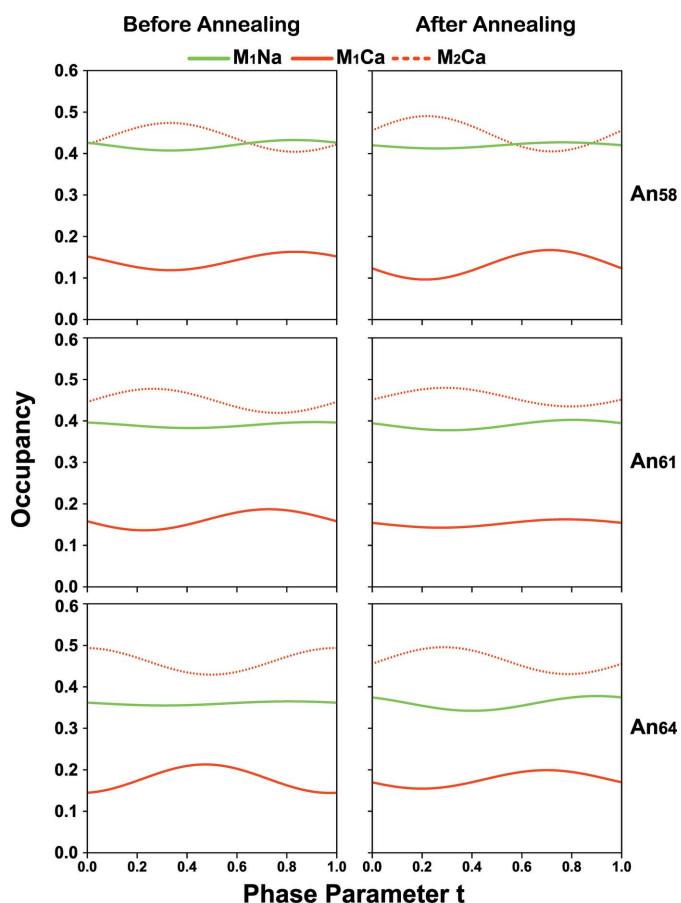


Figure 5
The occupancy modulation of the *M* sites in the three samples (MXCG-An₅₈, 96GM1-An₆₁ and Lake County-An₆₄). The amplitude in the *M* site occupancies does not change significantly after the two-week heating experiment, except for the Lake County sunstone sample which displays a phase shift in the modulation curve.

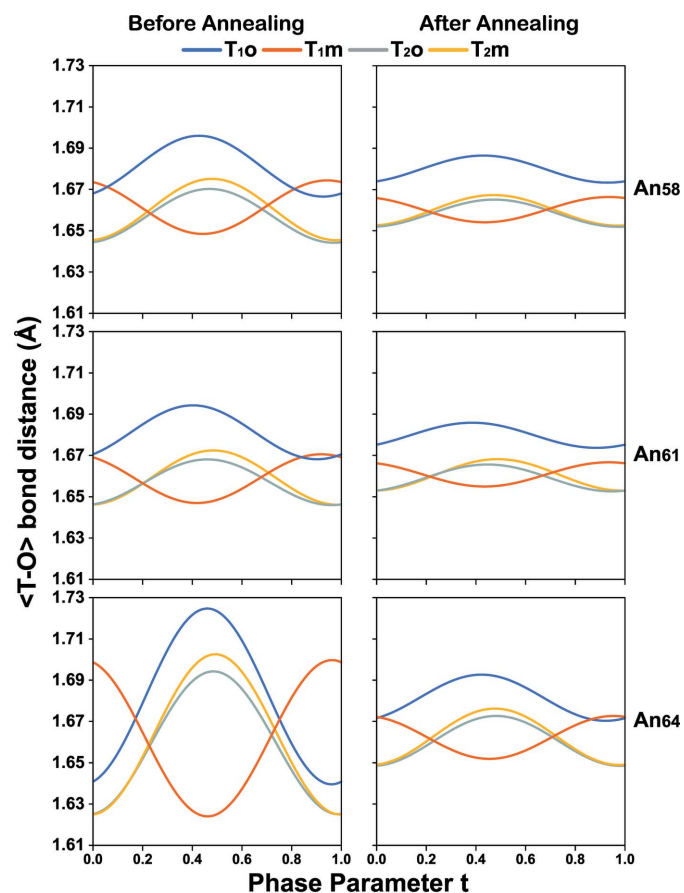


Figure 6
The $\langle T-O \rangle$ bond distance modulations of the three samples (MXCG-An₅₈, 96GM1-An₆₁ and Lake County-An₆₄). The amplitude of the (*T*–*O*) modulation obviously dropped after the samples were heated at 1100°C for two weeks, especially for the Lake County sunstone sample.

similar amplitude in the bond distance modulation. The Lake County sunstone sample shows a much larger amplitude compared to the other two, and is the largest amplitude ever observed in $e2$ structures. The modulation of the $\langle T-O \rangle$ bond distances noticeably dropped after heating for all the samples. The change in the Lake County sunstone sample after heating is the most dramatic. However, there is still about 0.03 Å variation left in the $\langle T-O \rangle$ bond distances in the Lake County sunstone sample, which is about the same as samples MXCG and 96GM1 before the heating experiment. The variation in the $\langle T-O \rangle$ distances after heating for samples MXCG and 96GM1, on the other hand, is about 0.014 Å, which is slightly more than samples 1974 ($An_{32.5}$) and 91315c (An_{35}) in previously published work (Jin & Xu, 2017a).

To best illustrate the incommensurately modulated structures and the changes after the heating experiment, Fig. 7 shows sections of the Lake County sunstone structure for before and after heating. The tetrahedra in the framework are coloured either blue and yellow for Al- and Si-dominated T -sites, respectively. The structure before the heating experiment shows obvious $e2$ ordering, with $I1$ -like domains (the red planes mark the centre of the $I1$ -like domain) connected by the $\bar{I}\bar{1}$ -like inversion twin boundary. The T -site ordering in the inversion twin boundary section of the structure shows obvious $\bar{I}\bar{1}$ -like ordering, with alternating Al and Si tetrahedra. This is an $e2$ structure with the longest modulation period ever reported. The structure after the heating experiment is clearly less ordered. Even though the centre of the $I1$ -like domains are marked with the red planes, it is hard to see any modulation in the structure. The structure is mostly a $C\bar{1}$ -

like disordered high albite structure, with all the Al-dominated T -sites being T_{10} . A small trace of modulation can be observed by carefully examining the T -site ordering pattern: the T_{10} sites near the red planes are all dominated by Al, whereas near the $\bar{I}\bar{1}$ -like inversion twin boundary, every other T_{10} site is dominated by Al. The modulation period almost halved after the heating experiment, and the orientation also changed dramatically. We have to emphasize that even though the coloured tetrahedra in the figure show different ordering patterns, both structures are strictly $e2$ structures, meaning the composition of the structure, both the bulk composition and local composition within each subcell, are exactly the same, the only difference is how the Al and Si atoms rearrange themselves within the subcell lattice.

5. *In situ* heating

The *in situ* heating experiment is designed to observe the change in the intensities of satellite peaks at different temperatures. Since most satellite reflections of the volcanic samples studied in this work are fairly weak, focus was only put on the most intense ones, such as the satellite peaks around the (071) position. A 180° fast scan of the heated single crystal was carried out, and the lattice parameters and crystal orientation matrix were calculated using the main reflections harvested from the screening. The frame which best captures the (071) reflection is located in the APEX2 program. A frame with 60 s 0.5° exposure was collected for each step during the *in situ* heating, and a final frame after the crystal cooled down to room temperature was collected. We tried to collect *in situ* heating diffraction data on all the samples used in this study. However, due to the limitations in the available heating equipment, only the measurement on the Hogarth Range sample was successful. The diffraction pattern of the Hogarth Range sample under different temperatures is shown in Fig. 8.

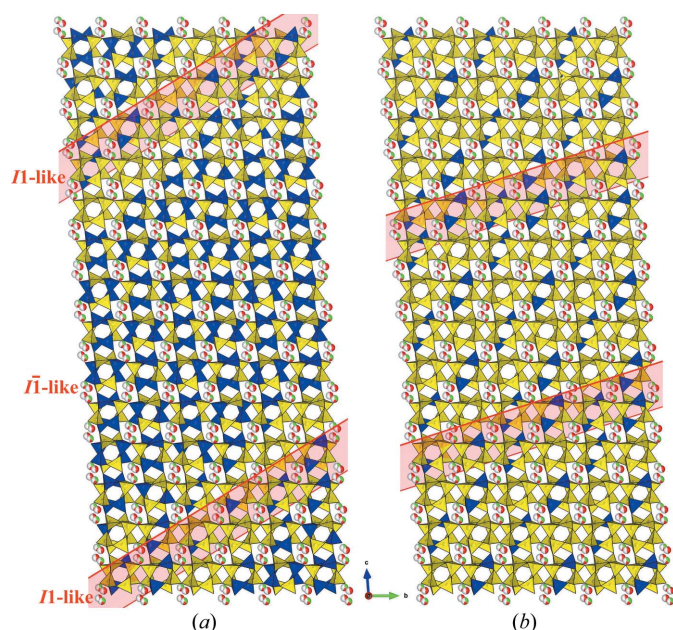


Figure 7
Sections (3×7 sub cells along b - and c -axes) of the incommensurately modulated structures of Lake County sunstone before (a) and after (b) the heating experiment. The tetrahedra are coloured blue and yellow for T -sites dominated by Al and Si respectively. The red planes mark the centre of the $I1$ -like domains.

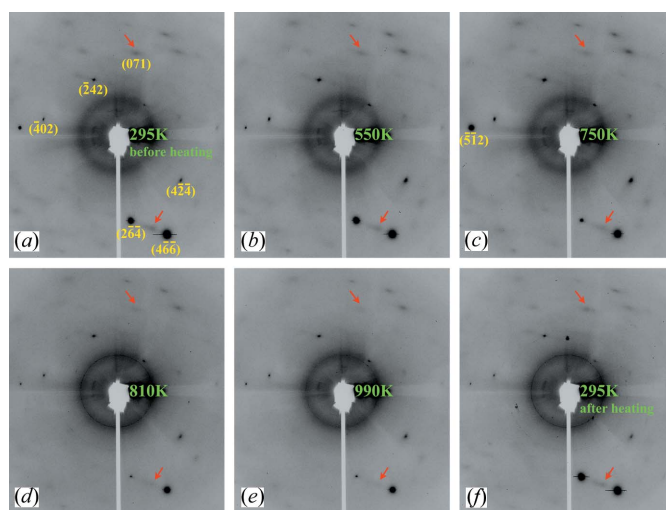


Figure 8
The *in situ* heating X-ray frames that contains (071) reflections. The data were collected at (a) 295 K, (b) 550 K, (c) 750 K, (d) 810 K, (e) 990 K and (f) 295 K again. The integrated peak profiles are plotted in Fig. 9.

As shown in Fig. 8, the satellite peak at the (071) position is quite diffuse but still obvious at room temperature. Another pair of satellite peaks at the ($4\bar{2}4$) position can also be observed in the same frame. The intensity of the satellite peaks did not obviously change at temperatures below 750 K. After the sample was heated to 810 K (537°C), an obvious drop in satellite intensity was observed. However, the satellite peaks did not completely disappear even after being heated up to 990 K, indicating some residual Al–Si ordering in the structure after annealing at 1100°C for two weeks. The intensities of the satellite peaks recovered to the original intensity after the temperature cooled below 750 K again. As shown in Fig. 8(f), the intensities of the satellite peaks are the same as in Fig. 8(a), but a sharp ring has appeared in Fig. 8(f) as a result of an artefact from the recrystallized silica capillary used to hold the sample. The evolution of the intensity profile of satellite peak around (071) position is plotted in Fig. 9, in which a gap among the peak profiles between 750 K and 810 K is clearly shown. The *in situ* heating experiment of the Hogarth Range sample provides strong evidence supporting the continuous and reversible nature of the initial transition between $C\bar{1}$ and *e*2 as suggested by Jin & Xu (2017a).

6. RUM analysis

Rigid Unit Modes (RUMs) are the normal modes in a polyhedral framework structure in which all the polyhedra in the framework oscillate as rigid units without any distortion in their shapes or sizes. RUM analysis is a powerful tool to study the displacive phase transitions in framework silicates (Tautz *et al.*, 1991; Dove *et al.*, 1995; Hammonds *et al.*, 1996; Withers *et al.*, 2002). With the *CRUSH* (Hammonds *et al.*, 1994) program, all the common framework silicates and aluminosilicates have been analyzed (Dove *et al.*, 1995; Hammonds *et al.*, 1996), and the displacive phase transition in tridymite, $\alpha\beta$ quartz and anorthite are proven to be related to the RUMs in the tetra-

hedral framework. The *CRUSH* program has also been used to analyze the fresnoite-type structures to explain the incommensurately modulated phase commonly observed in these layered framework structures (Withers *et al.*, 2002). The reciprocal *k*-points for RUMs in fresnoite-type structures calculated with *CRUSH* match almost exactly with the modulation wavevector measured from X-ray diffraction. This inspired us to try this method on the disordered volcanic plagioclase structures to see if the *e*-plagioclase structure is related to the RUMs, as the *in situ* heating experiment strongly suggests the displacive nature of the $C\bar{1}$ to *e*2 phase transition.

As the a^* -, b^* - and c^* -axes of the primitive reciprocal lattice of $C\bar{1}$ structures are almost equal in length, we simply divided the reciprocal lattice of the structures studied in this work into $100 \times 100 \times 100$ grids, and calculated the frequencies of all the modes for each grid point. Only the lowest frequency is considered for each point in reciprocal space, because other modes cannot be related to the RUM. After calculating the lowest frequency for all one million points in the reciprocal lattice, we can construct a 3D frequency map of the reciprocal space. The resulting resolution of the frequency map is about 0.0015 \AA^{-1} , which is very similar to that of the pseudo-intensity map presented by Dove *et al.* (2007). We did the same calculation for all four samples (heated) studied in this work, plus a low albite structure (Winter *et al.*, 1977) as a reference. The complete 3D frequency map can be found in the supporting information.

The results calculated for all four samples and the albite structure are very similar, indicating the RUM analysis is not sensitive to the slight change in the lattice parameters and tetrahedra sizes. Same as previously reported results (Hammonds *et al.*, 1996), the RUMs or QRUMs (quasi-RUM with close to zero frequency) can be found all over the reciprocal space. Surprisingly, none of the RUMs or QRUMs appear anywhere near the position of *e*-reflections in the reciprocal lattice. In fact, the frequencies around the *e*-reflections in reciprocal space are the highest. The reciprocal lattice of low albite and sample 96GM1 structure are illustrated in Fig. 10. The yellow isosurfaces show the region with

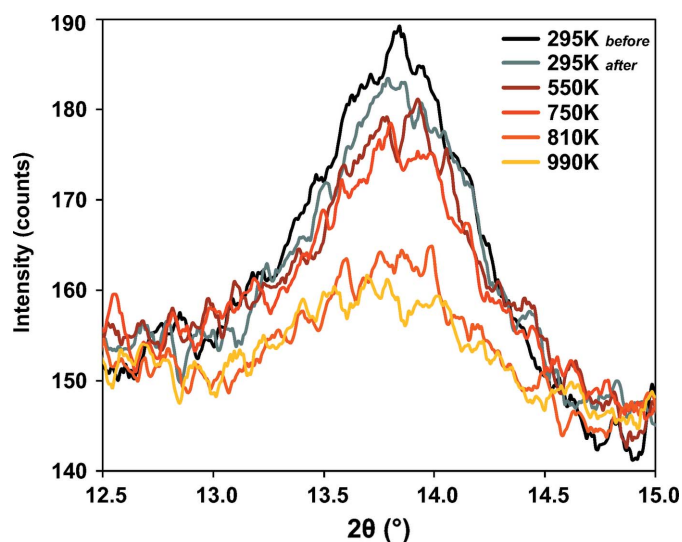


Figure 9
The intensity profiles of *e*-reflections around (071) position at different temperatures shown in Fig. 8.

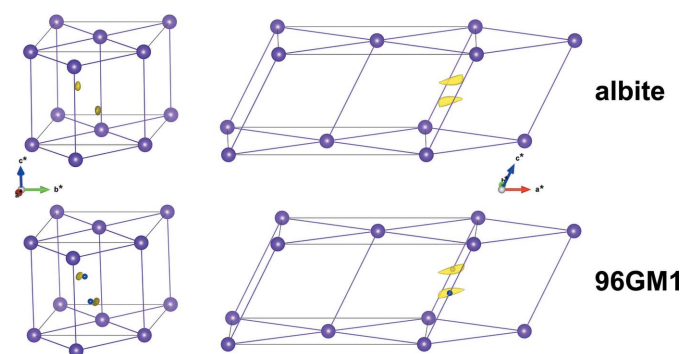


Figure 10
The reciprocal lattice of low albite (Winter *et al.*, 1977) and sample 96GM1 (heated). The position of the peak frequencies from the RUM analysis are marked with yellow isosurfaces in the frequency map. The position of *e*-reflections of sample 96GM1 measured from X-ray diffraction are marked by small blue balls in the lattice.

the highest frequencies in reciprocal space. The lattice points and the positions of *e*-reflections (measured from X-ray data) are marked by large purple balls and small blue balls, respectively. It is obvious that the positions of *e*-reflections are related to these frequency peaks in the reciprocal space, even though they do not overlap exactly. We call these high-frequency peaks in the RUM analysis ARUMs (anti-rigid unit mode), since they are the opposite of the RUMs. The fact that all four samples result in very similar RUM frequency distribution explains why the initial positions of the *e*-reflections seem to be the same for all compositions.

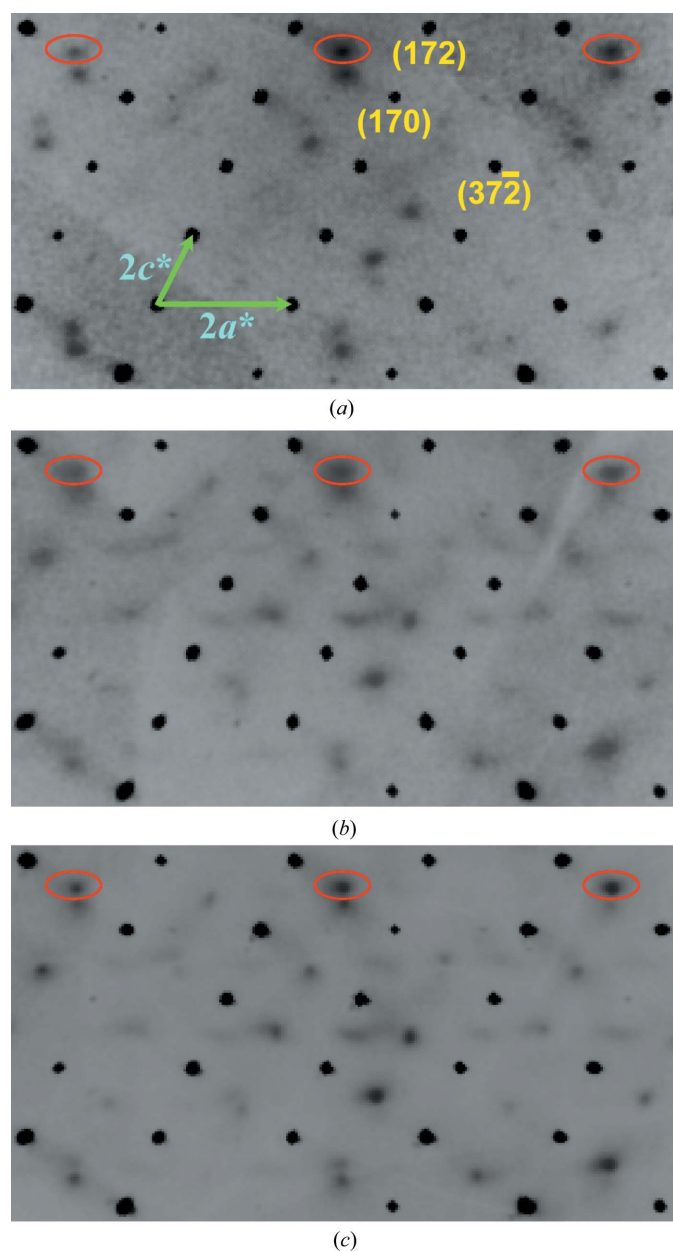


Figure 11
The *h7l* precession images of (a) sample 1974 (Jin & Xu, 2017a), (b) sample 96GM1 (after heating) and (c) sample 96GM1 (before heating). The elongation of the *e*-reflections (circled by red ovals) looks very similar to the shape of the frequency peaks shown in Fig. 10.

What is more surprising is that the shapes of the diffuse *e*-reflections in the X-ray diffraction resemble the shape of ARUM areas from the calculation. The *h7l* precession images of sample 1974 presented by Jin & Xu (2017a) together with sample 96GM1 (before and after heating) are shown in Fig. 11. The *e*-reflections in Figs. 11(a) and 11(b) are all elongated along the *a**-axis, which is the same as the ARUM area in Fig. 10. The *e*-reflections of sample 96GM1 before heating are fan-shaped, with the intensity more concentrated towards the *b*-position, as if the *e*-reflections are drawn closer as the structure gets more ordered.

7. Discussion

As proposed by Jin & Xu (2017a), the *e2* phase with no density modulation is not stable for compositions more calcic than An₄₄. The experiments by Carpenter and McConnell (Carpenter & McConnell, 1984; Carpenter, 1986) suggest only $C\bar{1}$ and $I\bar{1}$ structures are stable at high temperature, and the studies by Jin & Xu (2017a,b,c) support the stability of the *e1*-phase with density modulation (characterized by second-order satellites or *f*-reflections) at low temperature. However, evidence suggests that the boundary between $C\bar{1}$ and $I\bar{1}$ is a first-order transformation, thus the *e2* structure is more kinetically favourable compared to the $I\bar{1}$ structure, which explains why almost all plagioclase volcanic phenocrysts have *e2* structure (Jin, Wang & Xu, 2018; Vinograd *et al.*, 2001). A metastable phase boundary emphasizing the $C\bar{1}$ to *e2* transition is illustrated in Fig. 12, with the stable phase relations [put together from the results given by Jin & Xu (2017a,c) and Jin, Wang & Xu (2018)] marked with light-grey in the background.

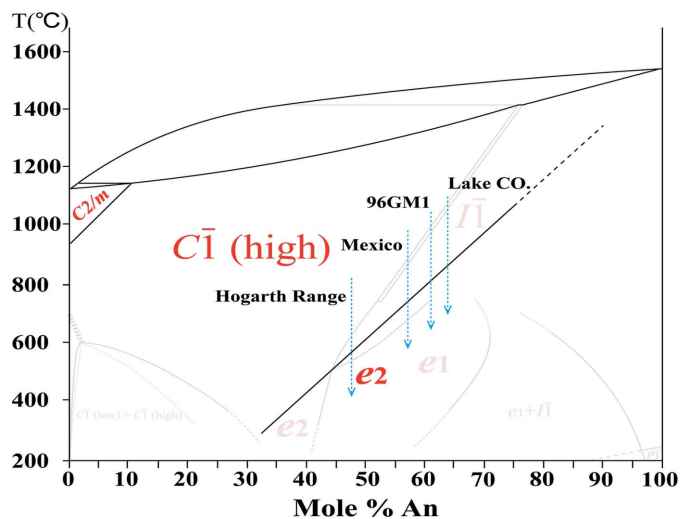


Figure 12
A schematic metastable phase diagram showing the relation between the $C\bar{1}$ and *e2* phases. The stable phase diagram put together from recently published results is shown as a greyed background in the figure. The composition and cooling paths of the four samples studied in this paper are also marked in the figure. The high-temperature region and the solvus for the Na-rich plagioclase feldspar (peristerite) are modified from Carpenter (1994).

It is really hard, if not impossible, to constrain the accurate position of the boundary between $C\bar{1}$ and $e2$ phases, due to the metastable nature of this transition. The exact transition temperature may also be dependent on the order parameter of the parent $C\bar{1}$ structure (Al occupancy in T_{10} site). We do not know whether the boundary would be a straight line or which direction should it curve towards. The straight line depicted in Fig. 12 is only schematic, roughly constrained by the stable phase relations proposed by Jin & Xu (2017*a,c*). We are almost certain that the transition temperature increases with increasing Ca component in the composition, since more calcic samples tends to be more ordered with stronger and sharper satellite reflections (Smith, 1983, 1984). Because the metastable $e2$ structure is only achievable by starting with a $C\bar{1}$ structure, the most calcic $e2$ in theory should be $\sim An_{75}$ (where the solid line terminates in Fig. 12), above which the plagioclase would directly crystallize as an $I\bar{1}$ structure and never turn to $e2$. However, the synthesized anorthite by Carpenter (1991) may suggest that a more calcic $e2$ structure can be achieved in extreme lab conditions such as annealing quenched glass with anorthite composition. Therefore, we extended the boundary with a dashed line to the anorthite end, even though we would never expect to see these anorthite with $e2$ structure preserved in nature.

The phase transformation from $C\bar{1}$ structure to $I\bar{1}$ structure is clearly driven by the Al–Si ordering, and recent research suggest it is a first-order transition instead of second order as previously believed (Jin, Wang & Xu, 2018). The excessive energy of anti-phase boundary during the phase transition could be the major inhibitor. In contrast, the transition to $e2$ has been believed to be mostly displacive, which would explain its preference over $I\bar{1}$ structure in rapidly cooled rocks. This is strongly supported by our *in situ* heating experiment, which shows instant and reversible change in the satellite intensity. However, the changes observed in the two-week annealing experiment suggest that Al–Si ordering plays an important role as well. The truth is, due to the static nature of the Al–Si disordering in the $C\bar{1}$ structure, it might be impossible to unambiguously discern an $e2$ structure from a completely disordered $C\bar{1}$ structure. The diffuse shadow around the e -position may always be there even at really high temperature, just like the almost ubiquitous c -reflections which we will discuss later.

To summarize our best understanding of the phase transition from $C\bar{1}$ to e . The transform initiates by displacement of the tetrahedral framework that forms small domains with an incommensurate wavevector around the ARUM area. The domain structure is likely to be driven by a local Al–Si distribution that is close to the e -ordering pattern (this does not require redistribution of Al and Si atoms in the framework, since there is a probability associated to any possible local ordering pattern in a truly disordered structure). Upon further cooling, Al and Si atoms would reorganize within the framework. This process happens relatively fast at a time scale of weeks or months, and it moves the modulation vector closer towards the b -position, resulting in a longer modulation period. As Jin, Wang & Xu (2018) pointed out, the $e2$ ordering

is easier than $I\bar{1}$ ordering in a $C\bar{1}$ parent structure, which would further prohibit $I\bar{1}$ structure from developing even though it is thermodynamically more stable. It is also not clear whether the change in modulation vector covers a continuous spectrum or not, but based on the limited data we have so far, the terminal q -vectors of $e2$ structure seem to be only dependent on the composition. The e -reflections studied in this paper seems to be the result of some kind of heterogeneous ordering [most obvious in Fig. 11(c)], where some domains are more ordered and display a sharper satellite peaks towards the terminal e -position, with still obvious residual diffuse scattering from the initial displacive transition that looks like a fan-shaped shadow. If a long enough annealing time is allowed within the $e1$ stable area [otherwise the $I\bar{1}$ structure would eventually prevail, as sample 28-88 in Jin, Wang & Xu (2018)], the Al–Si ordering would continue, followed by Ca–Na ordering, resulting in sharper and stronger e -reflections. And finally, the f -reflections would start to appear as the density modulation ordering happens, the structure equilibrates as an $e1$ structure with an $e2$ modulation period (same as sample SK90-12; Jin & Xu, 2017*c*).

The fact that e -ordering initiates around the ARUM area (Fig. 10) is quite counterintuitive and begs some explanation. RUMs are supposed to be how a polyhedral framework distorts without twisting individual polyhedra, and has been proven relevant in the incommensurate framework modulation of fresnoite-type structures (Withers *et al.*, 2002). To resolve this contradiction, we need to first review how the RUM analysis works. The most important part of the RUM analysis is simplifying a framework structure to a framework of rigid geometric objects connected by springs and get rid of all cations that are not part of the framework, which is a very different physical model than atoms connected by covalent and/or ionic bonds. Therefore, one should be very careful interpreting the results of the RUM analysis. It seems Winter *et al.* (1977) went too far by taking the oversimplified structural model too strictly, and suggested that the ‘complex subsolidus behaviour of feldspars’ can be explained by ‘local QRUMs’, which is the opposite of what we observed. The RUM analysis is mostly about the 3D geometric properties of a framework structure instead of the actual physical properties. With that in mind, we soon realize that the input plagioclase structure used for RUM analysis (disordered $C\bar{1}$ structure) is not a rigorous representation of the real plagioclase structure, but more of a spatial average of the real structure (*i.e.* none of the tetrahedra in the framework should be expected to have $\sim 1.67 \text{ \AA}$ $\langle T-O \rangle$ distances, but it is common in the average structure). This is how intermediate plagioclase is fundamentally different from fresnoite, quartz or even pure anorthite in the case of RUM analysis. If we compare the actual disordered plagioclase structure to the average structure from X-ray refinement, every single tetrahedron is distorted from the average structure (a Si tetrahedron is compressed and an Al tetrahedron is expanded compared to the average structure). So instead of trying to find a way to collapse the framework without twisting individual tetrahedra, the plagioclase structure would collapse in a

way that can accommodate the most distortions, which already exist in the parent disordered structure. Therefore, if RUMs and QRUMs can provide none-to-minimal polyhedron distortion, ARUMs should be where the most polyhedron distortion can be achieved. Actually, by this observation, the breathing RUM (BRUM) analysis (Goodwin *et al.*, 2006), where each polyhedron can expand and shrink relative to its average size seems more suitable in this case. However, this extra degree of freedom (DOF) would completely tip the balance between DOF and constraints in a tetrahedral framework, which would produce too many zero-frequency modes all over the reciprocal lattice, making the result impossible to interpret.

Another thing we need to discuss are the *c*-reflections ($h+k = \text{even}, l = \text{odd}$) that are almost always observed in the X-ray diffraction pattern of *e*-plagioclase. Before the controversial structure of *e*-plagioclase was solved and refined (Jin & Xu, 2017*b*), it was often believed that *c*-reflections are from

the *e*-plagioclase structure. However, a superspace group that produces both *e*-reflections and *c*-reflections would have a $c \sim 14 \text{ \AA}$ subcell but $C\bar{1}$ symmetry, and there has been no evidence suggesting that this type of subcell structure exists in plagioclase. Actually, the intensities of *c*-reflections in the heated MXCG sample seem to be very similar to those in the real $I\bar{1}$ structure of sample 55-88 (Jin, Wang & Xu, 2018), which suggests they are from local $I\bar{1}$ domains in the *e*-plagioclase crystal (which collapse to $P\bar{1}$ symmetry at low temperature). However, the *c*-reflections are also observed in the diffraction pattern of the Hogarth Range sample (Fig. 1), the composition of which is way out of the stable range of $I\bar{1}$ structure. What is more surprising is that the *c*-reflections are much more intense after the two-week heating than before [Figs. 13(*a*) and 13(*b*)] for the samples studied in this paper. Wenk (1978) also observed a similar trend where the *c*-reflections seem to be more prominent in less-ordered samples. As mentioned before, a truly disordered structure has a certain probability for any possible local arrangement. At high temperature, these random local arrangements would be masked by thermal vibration. However, at room temperature (or lower), where the X-ray diffraction data are collected, the local arrangements that resembles the $I\bar{1}$ structure would collapse to a local $P\bar{1}$ domain, which would be energetically more favourable. Actually, the more disordered the framework is, the higher the probability is for a local arrangement that is far from the average structure (*i.e.* a local $I\bar{1}$ -like arrangement), which explains the stronger *c*-reflections in the annealed sample. And as the *e*-ordering develops in the plagioclase structure, the probability of getting some local $I\bar{1}$ -like arrangement gets smaller and smaller. Almost no *c*-reflections can be observed in a fully ordered *e*1 structure such as sample 987L (Jin & Xu, 2017*c*) as shown in Fig. 13(*c*).

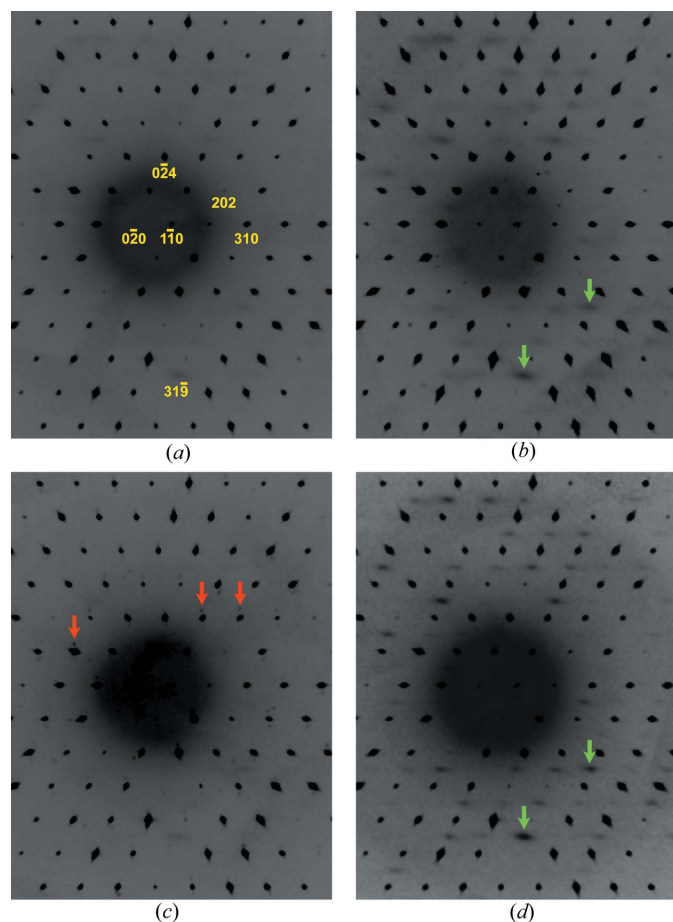


Figure 13
The $hh2l$ precession images of (*a*) sample MXCG (before heating), (*b*) sample MXCG (after heating), (*c*) sample 987L (Jin & Xu, 2017*b*) and (*d*) sample 55-88 (Jin, Wang & Xu, 2018). Sample 55-88 has a almost pure $I\bar{1}$ structure (green dot in Fig. 2) and is shown here for comparing the *c*-reflection intensities with the *e*-plagioclase samples. The pure *e*1 structure of sample 987L shows almost no *c*-reflections at all. Some *f*-reflections can be seen in this precession image of sample 987L as indicated by the red arrows. Some strong *c*-reflections such as 319 are indicated by green arrows.

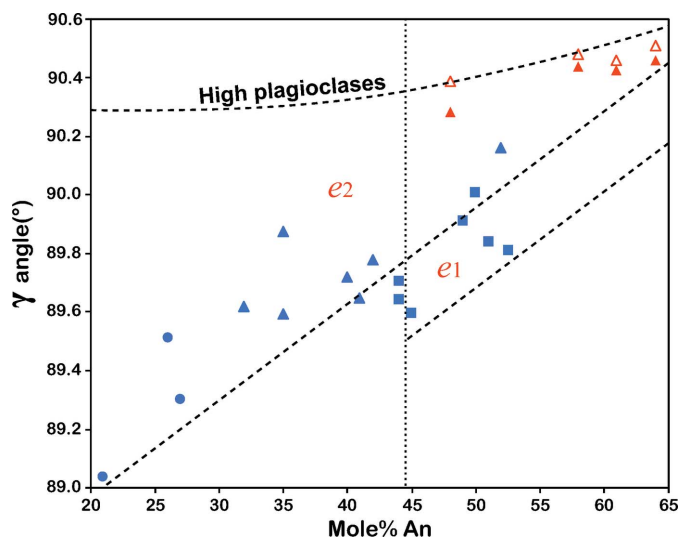


Figure 14
The γ angles of studied plagioclase structures plotted against the mole% An composition. The solid red triangles are the untreated natural samples and the unfilled red triangles are the heat-treated samples. The data points from Jin & Xu (2017*a*) are also plotted in blue colour for reference.

Table 4

The $\langle T-O \rangle$ distances (Å) of the average structures studied in this paper.

		T_{1o}	T_{1m}	T_{2o}	T_{2m}	Average
Hogarth Range (An ₄₈)	Untreated	1.681 (2)	1.656 (2)	1.653 (2)	1.655 (2)	1.661 (2)
	Annealed	1.675 (2)	1.656 (2)	1.657 (2)	1.656 (2)	1.661 (2)
MXCG (An ₅₈)	Untreated	1.682 (2)	1.661 (2)	1.657 (2)	1.660 (2)	1.665 (2)
	Annealed	1.680 (1)	1.660 (1)	1.659 (2)	1.660 (2)	1.665 (1)
96GM1 (An ₆₁)	Untreated	1.682 (1)	1.659 (1)	1.657 (2)	1.659 (2)	1.664 (1)
	Annealed	1.680 (1)	1.660 (2)	1.659 (2)	1.661 (2)	1.665 (2)
Lake County (An ₆₄)	Untreated	1.682 (1)	1.661 (1)	1.659 (2)	1.664 (2)	1.667 (2)
	Annealed	1.681 (3)	1.662 (3)	1.661 (3)	1.662 (4)	1.667 (3)

8. Conclusions and implications

Incommensurately modulated structures of basaltic phenocryst plagioclase crystals are accurately refined for the first time, through which the ordering states of these high-temperature structures are quantified by the amplitudes of the modulation wavefunctions. Heating experiments show that dramatic changes in the incommensurate ordering may be achieved in a relatively short period of time. Average occupancy in the T_{1o} site from neutron diffraction data shows no significant preference of Al, which suggests the $\langle T_{1o}-O \rangle$ distance is not a reliable reflection of Al occupancy for disordered $C\bar{1}$ structures. Rigid-Unit-Mode (RUM) analysis on the tetrahedral framework shows a connection between the e -reflections and Anti-RUM (ARUM), suggesting that the modulated structure initiates as a way to accommodate the internal strains introduced by the size discrepancy between Al and Si tetrahedra. Most importantly, this work confirms the metastable phase transition path between $C\bar{1}$ and $e2$ proposed by Jin & Xu (2017c), which explains the different characters of e -plagioclase in fast- and slow-cooled rocks.

Understanding the structural variations of volcanic samples can not only provide us with better understanding of the subsolidus phase relations of plagioclase solid solution series, it may also be a very powerful agent in studying the thermal histories of volcanic rocks. As shown by Jin & Xu (2017a), the interaxial angle γ of plagioclase structures is related to the Al–Si ordering of the framework. The γ angle generally decreases as the structure gets more ordered. However, as it was pointed out that the γ angle is more sensitive to the $\langle T_{1o}-O \rangle$ distance instead of the amplitude of modulation (Jin & Xu, 2017a). This poses a problem for using the γ angle to estimate the ordering state of a plagioclase structure. As shown in Fig. 14, the possible range for the γ angle of $e2$ -plagioclase with compositions more calcic than An₆₀ is fairly small. The γ angles of the Lake County sunstone sample before and after the annealing experiment are quite close, even though the modulation amplitude changed dramatically [Figs. 6(e) and 6(f)]. This supports the proposed relation between the γ angle $\langle T_{1o}-O \rangle$ distance, since the $\langle T_{1o}-O \rangle$ distance also barely changed after annealing (Table 4).

The results in this paper demonstrate that a short period time (relative to geological timescales) of annealing can change the $e2$ structure quite dramatically, especially for more calcium-rich samples. It is also known that the Al–Si ordering would essentially stop (or at least change extremely slowly) at

low temperature, so that the ordering states of ancient rocks are relatively well preserved. The amplitude of $\langle T-O \rangle$ distance modulation dropped from ~ 0.08 Å to ~ 0.02 Å in the Lake County sunstone sample after the annealing experiment. The reverse process, from a disordered to an ordered structure, may take a longer, but should be on a similar timescale. Therefore, in theory we can experimentally measure the structural change at different cooling rates, simply by starting with completely disordered $C\bar{1}$ structures (which can be prepared by annealing natural crystals at close to melting temperature), cool them down at controlled rates in an oven, and study the terminal structure. The shapes of satellite peaks, the distances between e -reflections (modulation periods) and even the intensity of c -reflections may also be used to evaluate the ordering state or cooling rate of the plagioclase feldspar.

Acknowledgements

Authors thank Dr John H Fournelle for providing the Hogarth Range sample and his assistance in the EPMA analyses. We thank Professor Andrew Goodwin from the University of Oxford for providing the modified *CRUSH* code (*B-CRUSH*) to calculate the BRUM in the plagioclase framework.

Funding information

The following funding is acknowledged: Center for Hierarchical Manufacturing, National Science Foundation (grant No. EAR-1530614 to Huifang Xu, Dane Morgan); Division of Scientific User Facilities, Office of Basic Energy Sciences, US Department of Energy (contract No. DE-AC05-00OR22725) with UT-Battelle, LLC; Argonne National Laboratory (contract No. DE-AC02-06CH11357). The neutron single-crystal diffraction measurement carried out at the Spallation Neutron Source was sponsored by the Division of Scientific User Facilities, Office of Basic Energy Sciences, US Department of Energy, under contract No. DE-AC05-00OR22725 with UT-Battelle, LLC. T Operation of PX² is supported by COMPRES (NSF EAR-1661511) and GSECARS (NSF EAR-1634415). This research used resources of the Advanced Photon Source, a US Department of Energy (DOE), Office of Science User Facility operated for the DOE Office of Science by Argonne National Laboratory under Contract No. DE-AC02-06CH11357. This study was also supported by the ORNL Graduate Opportunity (GO) Program.

References

- Angel, R. J., Carpenter, M. A. & Finger, L. W. (1990). *Am. Mineral.* **75**, 150–162.
- Arnold, O., Bilheux, J. C., Borreguero, J. M., Buts, A., Campbell, S. I., Chapon, L., Doucet, M., Draper, N., Ferraz Leal, R., Gigg, M. A., Lynch, V. E., Markvardsen, A., Mikkelsen, D. J., Mikkelsen, R. L., Miller, R., Palmen, K., Parker, P., Passos, G., Perring, T. G., Peterson, P. F., Ren, S., Reuter, M. A., Savici, A. T., Taylor, J. W., Taylor, R. J., Tolchenov, R., Zhou, W. & Zikovsky, J. (2014). *Nucl. Instrum. Methods Phys. Res. A*, **764**, 156–166.
- Carpenter, M. A. (1986). *Phys. Chem. Miner.* **13**, 119–139.
- Carpenter, M. A. (1991). *Am. Mineral.* **76**, 1110–1119.

- Carpenter, M. A. (1994). *Feldspars and Their Reactions*, Vol. 421, edited by Ian Parsons, pp. 221–269. Dordrecht: Kluwer Academic Publishers.
- Carpenter, M. A. & McConnell, J. D. C. (1984). *Am. Mineral.* **69**, 112–121.
- Chupas, P. J., Chapman, K. W., Kurtz, C., Hanson, J. C., Lee, P. L. & Grey, C. P. (2008). *J. Appl. Cryst.* **41**, 822–824.
- Dove, M. T., Heine, V. & Hammonds, K. D. (1995). *Mineral. Mag.* **59**, 629–639.
- Dove, M. T., Pryde, A. K. A., Heine, V. & Hammonds, K. D. (2007). *J. Phys. Condens. Matter*, **19**, 275209.
- Fitz Gerald, J. D., Parise, J. B. & Mackinnon, I. D. R. (1986). *Am. Mineral.* **71**, 1399–1408.
- Goodwin, A. L., Wells, S. A. & Dove, M. T. (2006). *Chem. Geol.* **225**, 213–221.
- Grove, T. L. (1977). *Am. Mineral.* **62**, 932–941.
- Grove, T. L., Ferry, J. M. & Spear, F. S. (1983). *Am. Mineral.* **68**, 41–59.
- Hammonds, K., Dove, M., Giddy, A. & Heine, V. (1994). *Am. Mineral.* **79**, 1207–1209.
- Hammonds, K. D., Dove, M. T., Giddy, A. P., Heine, V. & Winkler, B. (1996). *Am. Mineral.* **81**, 1057–1079.
- Horst, W. (1984). *Fortschr. Mineral.* **62**, 107–154.
- Horst, W., Tagai, T., Korekawa, M. & Jagodzinski, H. (1981). *Z. Kristallogr.* **157**, 233–250.
- Jin, S., Wang, X. & Xu, H. (2018). *Acta Cryst.* **B74**, 152–164.
- Jin, S. & Xu, H. (2017a). *Acta Cryst.* **B73**, 992–1006.
- Jin, S. & Xu, H. (2017b). *Am. Mineral.* **102**, 21–32.
- Jin, S. & Xu, H. (2017c). *Am. Mineral.* **102**, 1328–1339.
- Jin, S., Xu, H., Lee, S. & Fu, P. (2018). *Acta Cryst.* **B74**, 325–336.
- Kitamura, M. & Morimoto, N. (1977). *Phys. Chem. Miner.* **1**, 199–212.
- Kroll, H. & Ribbe, P. H. (1983). *Feldspar Mineralogy*, Vol. 2, edited by P. H. Ribbe, pp. 57–100. Washington, DC: Mineralogical Society of America.
- Kumao, A., Nissen, H.-U. & Wessicken, R. (1987). *Acta Cryst.* **B43**, 326–333.
- Langer, V. W. (1991). Masters Thesis. Oregon State University, USA.
- McConnell, J. D. C. (2008). *Can. Mineral.* **46**, 1389–1400.
- Momma, K. & Izumi, F. (2011). *J. Appl. Cryst.* **44**, 1272–1276.
- Nakajima, Y., Morimoto, N. & Kitamura, M. (1977). *Phys. Chem. Miner.* **1**, 213–225.
- Petríček, V., Dušek, M. & Palatinus, L. (2014). *Z. Kristallogr.* **229**, 345–352.
- Rainey, C. S. & Wenk, H.-R. (1978). *Am. Mineral.* **63**, 124–131.
- Schultz, A. J., Jørgensen, M. R. V., Wang, X., Mikkelsen, R. L., Mikkelsen, D. J., Lynch, V. E., Peterson, P. F., Green, M. L. & Hoffmann, C. M. (2014). *J. Appl. Cryst.* **47**, 915–921.
- Schultz, A. J., Srinivasan, K., Teller, R. G., Williams, J. M. & Lukehart, C. M. (1984). *J. Am. Chem. Soc.* **106**, 999–1003.
- Smith, J. V. (1983). *Rev. Mineral.* **2**, 223–239.
- Smith, J. V. (1984). *Feldspars and Feldspathoids*, Vol. 137, edited by W. L. Brown, pp. 55–94. Dordrecht: Reidel Publishing Company.
- Smith, J. V. & Ribbe, P. H. (1969). *Contrib. Mineral. Petrol.* **21**, 157–202.
- Stewart, D. B., Walker, G. W., Wright, T. L. & Fahey, J. J. (1966). *Am. Mineral.* **51**, 177–197.
- Tagai, T., Joswig, W., Korekawa, M. & Wenk, H.-R. (1978). *Acta Cryst.* **A34**, S183–S183.
- Tagai, T. & Korekawa, M. (1981). *Phys. Chem. Miner.* **7**, 77–81.
- Tautz, F. S., Heine, V., Dove, M. T. & Chen, X. (1991). *Phys. Chem. Miner.* **18**, 326–336.
- Vinograd, V. L., Putnis, A. & Kroll, H. (2001). *Mineral. Mag.* **65**, 1–31.
- Wenk, H.-R. (1978). *Am. Mineral.* **63**, 132–135.
- Wenk, H.-R., Joswig, W., Tagai, T., Korekawa, M. & Smith, B. K. (1980). *Am. Mineral.* **65**, 81–95.
- Wenk, H.-R. & Nakajima, Y. (1980). *Phys. Chem. Miner.* **6**, 169–186.
- Winter, J. K., Ghose, S. & Okamura, F. P. (1977). *Am. Mineral.* **62**, 921–931.
- Withers, R. L., Tabira, Y., Liu, Y. & Höche, T. (2002). *Phys. Chem. Miner.* **29**, 624–632.
- Xu, H. (2015). *Am. Mineral.* **100**, 510–515.
- Xu, H., Jin, S. & Noll, B. C. (2016). *Acta Cryst.* **B72**, 904–915.
- Zhang, D., Dera, P. K., Eng, P. J., Stubbs, J. E., Zhang, J. S., Prakapenka, V. B. & Rivers, M. L. (2017). *J. Vis. Exp.* **119**, e54660.
- Zikovsky, J., Peterson, P. F., Wang, X. P., Frost, M. & Hoffmann, C. (2011). *J. Appl. Cryst.* **44**, 418–423.